Experimental study and attitude control of a floating type shrouded wind turbine

Zhu, Hongzhong
Research Institute for Applied Mechanics, Kyushu University

Sueyoshi, Makoto
FREGATA TECH LLC

出版情報：Sustainable Energy Technologies and Assessments. 50, pp.101811-, 2022-03. Elsevier
バージョン：
権利関係：

Experimental Study and Attitude Control of a Floating Type Shrouded Wind Turbine

Hongzhong Zhu[a,*], Makoto Sueyoshi[b]

[a]*Research Institute for Applied Mechanics, Kyushu University, Kasuga 816-8580, Japan*
[b]*FREGATA TECH LLC, Buzen 828-0066, Japan*

Abstract

Thrust force needs to be taken into account in the development of floating type shrouded wind turbines since it would lead to large tower inclination, and both the power conversion efficiency and the safety margin of the system would be reduced. In this study, a novel spar-type shrouded wind turbine using a hinge to mount the nacelle on the tower, which can maintain the nacelle in horizontal state even with large tower inclination, is studied based on a 1:100 model. The characteristics of the wind turbine are studied via wind tunnel experiments and wave basin experiments. In wind tunnel experiments, the wind speed-up performance of the shroud and the self-aligning property of the wind turbine are evaluated. In wave basin experiments, dynamical response of the wind turbine in idling, operational and parked modes are studied. A model-based attitude controller for stabilizing the nacelle is also proposed and the control performance is analyzed based on experimental results.

Keywords: floating shrouded wind turbine; cyclic pitch control; attitude control; wind tunnel experiments; wave basin experiments

1. Introduction

With the development of wind turbine technologies, wind energy has become one of the fastest growing renewable energy resources. Since 1990, wind power has increased at an average compound annual growth rate of more than 20% [1]. At the end of 2018, the global install wind capacity reached 564 GW and the wind power's share of worldwide electricity usage reached 4.8% [2]. The International Energy Agency (IEA) targets 15% to 18% share of global electricity from wind power by 2050 in its roadmap, and floating offshore wind energy is recognized as an important component part for addressing the targets [3]. Industry experts estimate that around 5 GW to 30 GW of floating wind power could be installed worldwide by 2030 [4].

*Corresponding author
Email addresses: zhuhongzhong@riam.kyushu-u.ac.jp (Hongzhong Zhu), sueyoshi@fregata.tech (Makoto Sueyoshi)

A wind turbine shrouded a properly designed duct can aid the turbine to reach the Betz limit and also may surpass it [5, 6, 7, 8]. Therefore, shrouded wind turbines have become a significant part of current research agendas since they can provide a promising solution for improving the efficiency and economic feasibility of power production even from low energy density flows [9, 10, 11, 12]. Nevertheless, the large drag force working on the shroud, which would raise the manufacturing cost, also becomes an influential problem for industrial applications [13, 14]. Especially, a large floating foundation with high restoring capacity is necessary to neutralize the drag force on the shroud [15, 16].

In order to reduce the drag force, several innovative methodologies have been proposed in the literature. Siavash *et. al* published a study on implementing a foldable diffuser for a micro scale wind turbine [13, 17]. The diffuser is equally partitioned into movable parts and unmoved parts, and capable to be half-open to reduce the aero loads in high wind conditions. In [18], a self-adaptive flanged diffuser which can automatically reduce the projected area of the flange under high wind speeds has been proposed. Numerical study showed that a 35% drag force reduction could be obtained at a wind speed of 60 m/s. In addition, efforts have also been made on applying optimization methods for shroud geometry design considering both the speed-up ratio and drag force reduction [19].

Studies on reducing the effects of the drag force are another research agendas. In [20] and [21], a spar-type shrouded wind turbine concept using a revolute hinge to mount the nacelle on its supportive tower has been proposed. By the hinge mechanism, the nacelle can be maintained in horizontal state even under large tower inclination. The method can not only improve the output performance of the wind turbine but also reduce the stress between the nacelle and the tower. In addition, a novel mooring system was proposed in the studies so that the mobility of the wind turbine would be improved. A modeling approach has been proposed to study the system under various environment conditions.

In order to confirm the aero-hydro feature of the wind turbine, a 1:100 small-scale model is developed, and model tests are performed in this study. In the remainder of this paper, firstly, the properties of the model are presented. Then, wind tunnel tests and wave basin tests are performed and their results are reported. Finally, an attitude controller for stabilizing the nacelle in both operational mode and parked mode is designed and implemented, and the motion response of the wind turbine is discussed.

2. Experimental System

The experimental model is the 1:100 model of a 500kW wind turbine, and its overview is shown in Fig. 1. The floater is an advanced spar-type floater consists of a lightweight pontoon and a weight. Guy wires and a slender beam are employed to install the weight under the pontoon. By the configuration, the gravitational restoring performance can be improved since the buoyancy is shifted upward whereas the center of mass of the turbine is maintained at a low position. In full-scale system, the floater can be simplified to consist of a short spar (filled with ballast water) and a cylindrical column, as discussed in [20].

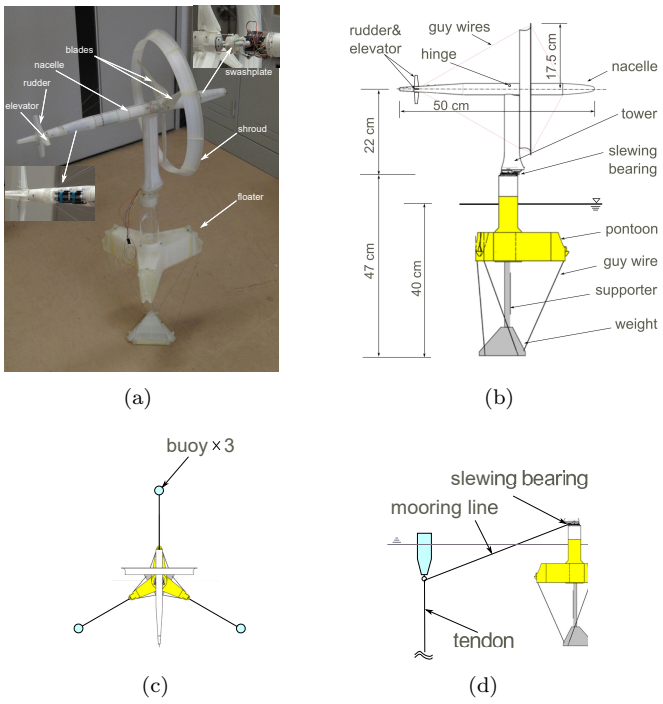

Figure 1: Overview of experimental shrouded wind turbine: (a) experimental model, (b) profile and dimensions, (c) topview of mooring system, and (d) sideview of mooring system.

The cross section of the tower is designed as a thin symmetrical airfoil to reduce the tower shadow effects. The nacelle is mounted on the tower via a revolute hinge (a shaft with two supportive ball bearings). The shroud is installed on the nacelle via 10 sets radially distributed tensioned guy wires. In the upwind side, the wires are connected to the nacelle with a small angle (30 deg to the nacelle axis) to tangle with the wind drag on the shroud. In the downwind side, the wires are connected to the nacelle with a large angle (75 deg to the nacelle axis) to overcome the gravitational force. This mechanism can be consulted to the rim of ferris wheels. Rudder and elevator are mounted on the upwind side of the nacelle to help on regulating the orientation and attitude of the wind turbine. Furthermore, a swashplate is applied to regulate the collective and cyclic pitch angle of the blades.

The mooring system consists of three one-legged tension-leg-platform (TLP) buoys, a slewing bearing (installed on the floater top), and three sets of mooring lines. The overview of the mooring system is shown in Fig. 1(c,d). The slewing bearing enables the wind turbine to have the flexibility to align itself to track the wind direction. In order to reduce the coupling effects between the TLP buoys and the wind turbine, the connection points of the mooring lines are set at the bottom of the buoys. In practical situation, gravitational anchors would

Table 1: Properties of experimental model.

Property	Value
Rotor mass (include gearbox) (g)	70
Shroud mass (g)	70
Nacelle mass (g)	210
Tower mass (g)	70
Floater mass (g)	1480
Buoy mass (g)	51
Tower height (cm)	29
Center of mass of floater (cm)	-28.2
Displacement of floater (cm^3)	1900
Displacement of buoy (cm^3)	230
Center of buoyancy of floater (cm)	-14.8
Distance between buoys (cm)	130
Elevator/rudder area (cm^2)	6
Water plane area of floater/buoy (cm^2)	19.6
Hinge to the nacelle central line (cm)	0.75

be applied for securing the TLP buoys. By the consideration, the anchors can be winched up so that the removal of the system would become an energy-saving work. This feature can largely improve the mobility of the wind turbine, and the system would therefore be applicable as a temporary power source for offshore construction use.

The experimental model are made of synthetic resin by a high-precision 3D printer (Projet3500HDMax), and the properties of the system are listed in Table 1. To measure the motion of the floating wind turbine, two inertial measurement units (MPU-6050™) are installed in the nacelle and the floater. A small dc motor having rated speed of 22,000 rpm is applied to control the rotor rotational speed. Pulse width modulation (PWM) -driven digital servos (ES 9251, made by EMAX) are applied to drive the rudder, elevator and blades. In addition, a computer-on-module (Intel® Edison Breakout Board Kit) is utilized for signal processing and controller implementation.

3. Wind Tunnel Experiments

A large atmospheric boundary layer wind tunnel installed at the Research Institute for Applied Mechanics in Kyushu University is applied for evaluating the performance of the wind turbine. The experimental setup are shown in Fig. 2. The tower is fixed on a 6-component strain gauge. The hinge between the nacelle and the tower is disabled so that the nacelle can be kept still in horizontal level. A shield is applied to cover the base of the turbine to reduce the blockage effects caused by the tower base.

The speed-up ratio of the shroud is firstly explored. In the tests, the blades, elevator and rudder are removed from the wind turbine and the nacelle is placed

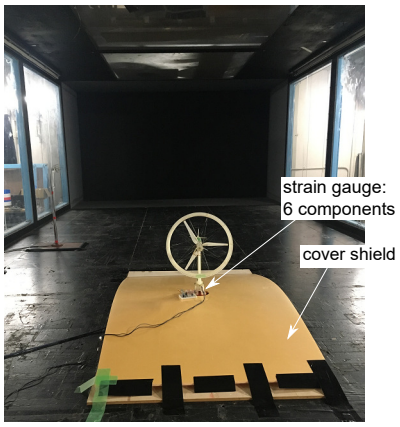

Figure 2: Overview of wind tunnel and scenery of wind tunnel tests.

in parallel with the wind direction. The inflow wind speed is set as 5 m/s so that the Reynolds number based on the diameter of the shroud is about 1.2×10^5. A hot-wire probe placed normal to winds is applied to measure the wind speeds at rotor plane. The normalized results are shown in Fig. 3(a). In the figure, the term U_∞ is the inflow wind speed, u is the local wind speed, R is the radius of rotor, and r is the location of the probe. It can be observed that the wind speed is amplified by 10% near the nacelle and 30% near the shroud. By calculation, the overall air flow rate at rotor plane increases by 20%.

The characteristics of the wind turbine with respect to tip-speed ratio, collective pitch, cyclic pitch and wind-wind turbine misalignment are also studied. The power coefficient C_p, thrust coefficient C_t, yawing moment coefficient C_m and cyclic pitching moment coefficient C_c are applied for the analysis. The coefficients are defined as follows:

$$C_p(\lambda, \beta) = \frac{P}{\frac{1}{2}\rho_a A U_\infty^3}, \tag{1}$$

$$C_t(\lambda, \beta) = \frac{T}{\frac{1}{2}\rho_a A U_\infty^2}, \tag{2}$$

$$C_m(\psi) = \frac{M_\psi}{\frac{1}{2}\rho_a A R U_\infty^2}, \tag{3}$$

$$C_c(\gamma) = \frac{M_c}{\frac{1}{2}\rho_a A R U_\infty^2}, \tag{4}$$

where ρ_a is the air density, A the rotor plane area (swept area of blades), $\lambda = \frac{\Omega R}{U_\infty}$ the tip-speed ratio, β the collective blade pitch, ψ the yaw angle of the turbine, γ the cyclic pitch, P the generator power, T the thrust, M_ψ the yaw moment caused by the wind-wind turbine misalignment, and M_c the pitching moment of the rotor under cyclic pitch.

The inflow wind speed is set as $U_\infty = 1.5$ m/s, and the rotor speed Ω is

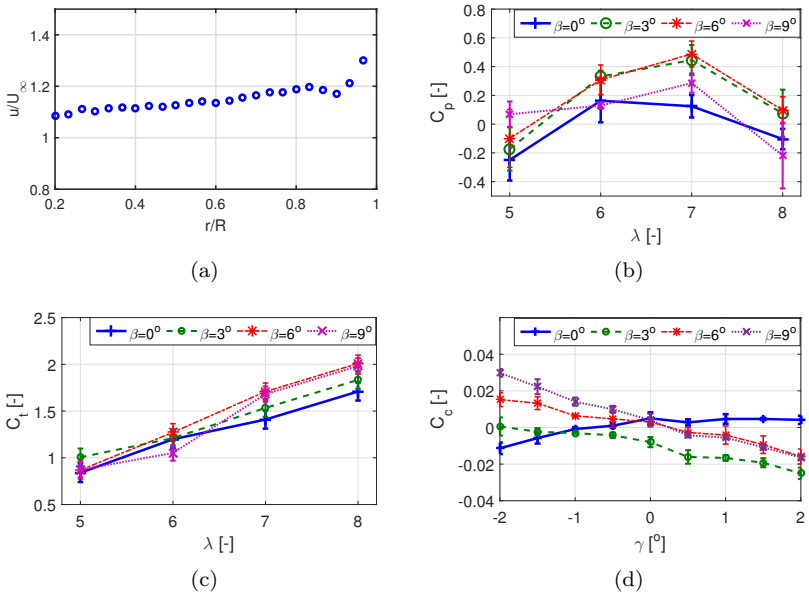

Figure 3: Results of wind tunnel experiments: (a) Speed-up performance by the shroud, (b) Power coefficients, (c) thrust coefficients, and (d) Cyclic pitching moment coefficient.

controlled to let the tip-speed ratio λ be $\lambda \in [5,\ 6,\ 7,\ 8]$. The blade collective pitch command β is regulated as $\beta \in [0^o,\ 3^o,\ 6^o,\ 9^o]$. To reduce the hysteresis effect of the swashplate, the blade pitch is driven to the designated angles from both sides and therefore two experiments are carried out for each pitch angle. A 60-second-long measurement is recorded for each experiment and the mean and standard deviation of the measurement are analyzed. The power coefficient and thrust coefficient as a function of λ are shown in Fig. 3(b,c). It can be found that the maximum power coefficient appears around ($\lambda = 7,\ \beta = 6^o$). In addition, the thrust coefficient can be estimated to vary almost linearly with λ under the experimental conditions.

The rotor pitch moment caused by the cyclic pitch angle γ is investigated by varying the cyclic pitch command value γ in $[-2^o,\ 2^o]$ with a step size of 0.5^o, and the results are shown in Fig. 3(d). In small cyclic pitch angles, it can be found that the pitch moment coefficient changes almost linearly with γ. This would remarkably reduce the design complexity of cyclic pitch controller since controller design technologies for linear system, such as Proportional-Integral-Derivative (PID) control, are almost mature and easy to use.

The restoring moment under wind-wind turbine misalignment is studied by setting the yaw angle of the wind turbine from 0^o to 180^o with a step size of 5^o. The schematic view of the experiments and the resulted yaw moment coefficient are shown in Fig. 4. The negative quantity of C_m indicates that the wind turbine can generate a restoring moment against the wind-wind turbine

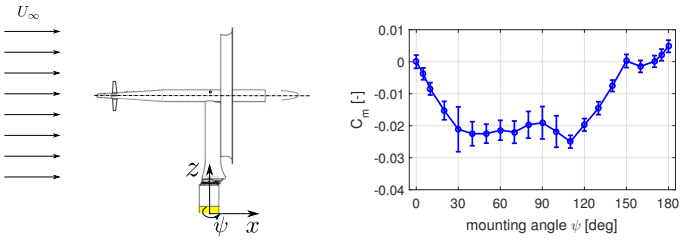

(a) (b)

Figure 4: Static moment in yaw with respect to the incident angle in wind tunnel tests.

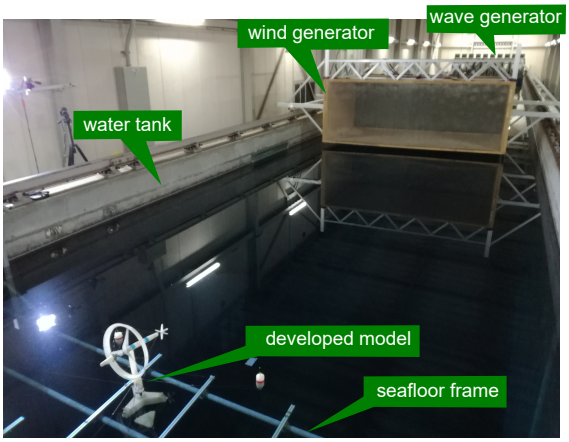

Figure 5: Overview of model tests in water tank.

misalignment. From the results, it can be found that the self-aligning property can be preserved when $\psi \in [0^o, 150^o]$ (and $[210^o, 360^o]$ by taking account of the geometric symmetry). In practical situation, rudders installed on the upwind side of the nacelle can be applied to help on aligning the wind turbine when the wind travels from the opposite direction. Therefore, the wind turbine can be regarded that it can align itself passively towards the wind direction by the aforementioned design.

4. Wave Basin Experiments

To explore the characteristics of the wind turbine, such as the natural frequencies and the motion feature under aero- and hydro- dynamics, wave basin experiments are carried out. The water tank with length 65 m, width 5 m and depth 7 m installed at the Research Institute for Applied Mechanics (RIAM) of Kyushu University is applied, and the overview of the setup is shown in Fig. 5. The wind generator is composed of 12 axial flow fans and able to generate a maximum average wind speed of 5 m/s. The wave generator is of plunger type

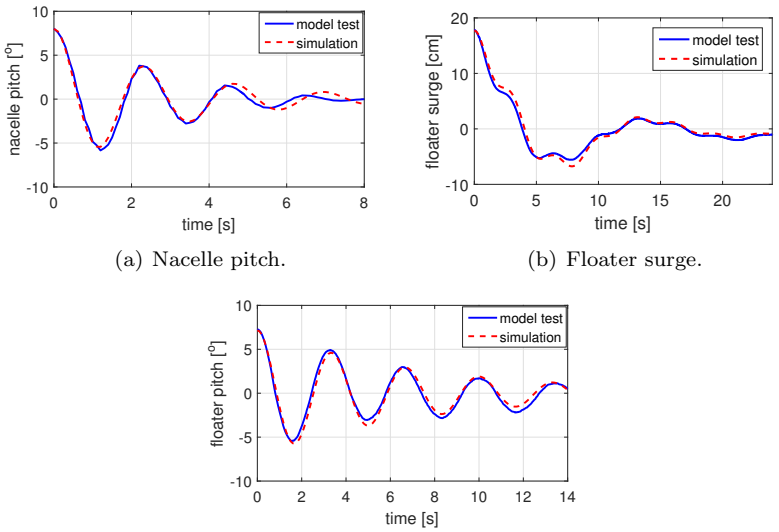

(a) Nacelle pitch.

(b) Floater surge.

(c) Floater pitch.

Figure 6: Comparison of the free decay results.

Table 2: Natural frequencies and damping ratios of the experimental model.

	nacelle	floater with wind turbine (hinge fixed)		
	pitch	surge/sway	heave	roll/pitch
natural frequency [rad/s]	2.75	0.45	2.26	2.23
damping ratio [-]	0.12	0.30	0.12	0.078

and is capable to generate regular waves with a maximum wave height of 0.3 m. A movable sea floor frame for installing the mooring system is assembled in the water at a depth of 0.9 m. A set of high-speed stereo cameras is applied to capture the motion of the wind turbine. In the experiments, winds and waves travel in the same direction along the positive x-axis.

4.1. Free Decay Response

Free decay experiments are performed to analyze the natural frequencies and damping ratios of the floating wind turbine. The experiments are performed by settling the initial position of each motion DOF away from its equilibrium state, and then let the system move freely on water. The results in time-series are shown as the solid lines in Fig. 6. As the floater motion in sway and roll DOFs are very similar to the motion in surge and pitch DOFs, respectively, their results are omitted in the figure. From the experiments, it can be found that the motion oscillate periodically and decay with time. The natural frequencies as well as the damping ratios can be estimated from the experiments and the results are compared in Table 2.

Table 3: Wind and wave conditions in wave basin experiments.

wind speed and turbine mode	wave	
	wave period [s]	wave height [mm]
	0.65	10
0.0 m/s, idling	0.75	15
1.6 m/s, operational	0.90	25
4.0 m/s, parked	1.00	30
	1.20	35
	1.50	40

4.2. Motion Response in Winds and Waves

The wind turbine in idling, operational, and parked modes is studied, and the wind speeds are set as 0.0 m/s, 1.6 m/s, and 4.0 m/s, respectively. In the operational mode, the collective pitch is set as $\beta = 9^o$ and the rotor rotational speed is controlled to let the tip-speed ratio be $\lambda = 6$. The cyclic pith, elevator and rudder are not controlled during these experiments. The marine environment around Tohoku Pacific Coast Area of Japan [22] is considered, and the wave conditions for the experiments are given in Table 3.

In each experiment, a 30-wave periods-long measurement is recorded after the transient response. The dynamics of the experimental model are analyzed based on motion response amplitude operators (RAOs), as shown in Fig. 7. In the figure, ζ_a is the wave amplitude, k_a the wave number, λ_w the wave length, D the diameter of the floater at still water level, Θ_n, X_f, Z_f and Θ_f the motion amplitude of the nacelle in pitch, the motion amplitude of the floater in surge, heave and pitch DOFs, respectively. It can be found that the motion RAOs in the idling mode and the operational mode are not recorded much different from each other. These results indicate that the motion of the wind turbine are mainly affected by waves under low and moderate wind speeds. In the parked mode with high wind speed, the pitch motion of the nacelle becomes large, especially in low-frequency waves. This would be caused by the fact that the natural frequency of the nacelle in pitch DOF increases under high wind speeds and approaches to the wave-frequency zone. A theoretical explanation of this point of view will be explained in Section 5.1. The large aero-force on the wind turbine also induces a large floater motion in pitch DOF, as illustrated in Fig. 7(d). On the other hand, the floater motion RAOs in surge and heave DOFs are, conversely, reduced in the parked mode. High wind speed leads to large floater displacement in surge DOF, and results to a large tendon tilt. The restoring coefficients in surge and heave DOFs are enhanced by the mooring system, and therefore their wave-induced motion are restrained.

From the experiments, it is observed that the nacelle pitch motion need to be stabilized, especially under high wind speeds. In the following, a numerical model for controller design is presented, and the effectiveness of the controller is discussed.

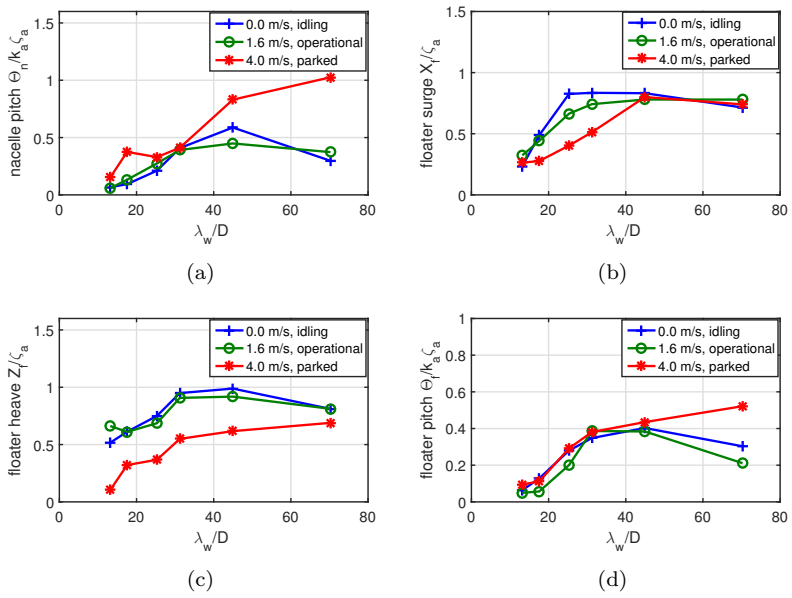

Figure 7: Motion response of the wind turbine model under three wind turbine modes: (a) nacelle in pitch DOF, (b) floater in surge DOF, (c) floater in heave DOF, and (d) floater in pitch DOF.

5. Nacelle Attitude Control

In this section, the cyclic pitch and the elevator will be applied to regulate the nacelle pitch motion. In order to reduce the complexity of the controller design, some assumptions are given in advance:

- The gyroscopic resistance caused by the rotor rotation is omitted so that gyroscopic properties would not affect the motion of the nacelle and floater.
- The flexibility between the nacelle and the shroud can be neglected.

Based on the assumptions, the floating wind turbine is regarded to be composed by a supporter and a lever arm, as shown in Fig. 8. The supporter consists of the floater and tower whereas the lever arm includes the nacelle, shroud and rotor.

5.1. Numerical Model

The governing equations of motion can be obtained by *Lagrange's equation*:

$$\frac{\mathrm{d}}{\mathrm{d}t}\left(\frac{\partial L}{\partial \dot{q}_i}\right) - \frac{\partial L}{\partial q_i} = Q_i \tag{5}$$

where $L = T - U$ is the *Lagrangian*, which is the combination of the kinetic energy T and potential energy U, q_i the i^{th} generalized coordinate, and Q_i the i^{th} generalized external force.

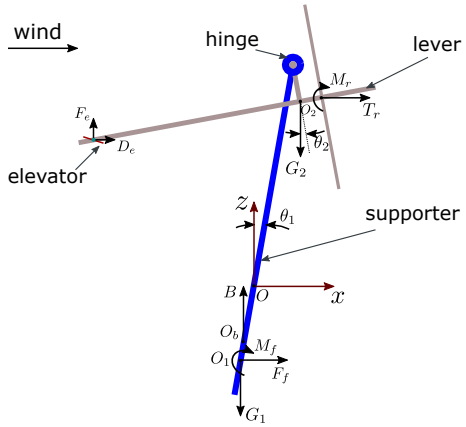

Figure 8: Simplified structural model of the wind turbine.

Considering the motion of the turbine in xz-plane, the kinetic energy (including the fluid kinetic energy [23]) as well as the potential energy can be expressed by

$$T = \frac{1}{2}m_1\dot{x}_1^2 + \frac{1}{2}I_1\dot{\theta}_1^2 + \frac{1}{2}m_2(\dot{x}_2^2 + \dot{z}_2^2) + \frac{1}{2}I_2\dot{\theta}_2^2 + \frac{1}{2}\boldsymbol{v}_f M_a \boldsymbol{v}_f, \tag{6}$$

$$U = m_2 g z_2, \tag{7}$$

where $\boldsymbol{v}_f = [\dot{x}_1,\ \dot{\theta}_1]^T$ is the velocity vector of floater, m_1 and m_2 the supporter mass and lever mass, respectively, I_1 and I_2 the moment of inertia of the supporter and lever, respectively, g the gravitational acceleration, and M_a the added mass matrix. The position of the lever can be expressed by

$$x_2 = x_1 + \ell_1 \sin\theta_1 - \ell_2 \sin\theta_2, \tag{8}$$

$$z_2 = \ell_1 \cos\theta_1 - \ell_2 \cos\theta_2, \tag{9}$$

where ℓ_1 is the distance between O_1 and the hinge, and ℓ_2 is the distance between O_2 and the hinge. In addition, the term M_a can be expressed by

$$M_a = \begin{bmatrix} X_{\ddot{x}_1} & X_{\ddot{\theta}_1} \\ P_{\ddot{x}_1} & P_{\ddot{\theta}_1} \end{bmatrix}, \tag{10}$$

where $X_{\ddot{x}_1}$ is the added mass of the floater in surge, $P_{\ddot{\theta}_1}$ the added moment of inertia in pitch, $X_{\ddot{\theta}_1}$ and $P_{\ddot{x}_1}$ ($X_{\ddot{\theta}_1} = P_{\ddot{x}_1}$) the coupled added mass and moment of inertia between surge and pitch.

Choosing the generalized coordinates be $\boldsymbol{q} = [x_1,\ \theta_1,\ \theta_2]^T$ and considering $\theta_1 = \theta_{10} + \theta_f$ (θ_{10} is the equilibrium inclination angle and θ_f is the small perturbation), the system can be expressed as

$$\Xi\ddot{\boldsymbol{p}} + \Gamma\boldsymbol{p} = \boldsymbol{Q}. \tag{11}$$

where $\boldsymbol{p} = [x_1,\ \theta_f,\ \theta_2]^T$, Ξ and Γ are expressed by

$$\Xi = \begin{bmatrix} m_1 + m_2 + X_{\ddot{x}_1} & P_{\ddot{x}_1} + X_{\ddot{\theta}_1} + m_2\ell_1\cos\theta_{10} & -m_2\ell_2 \\ P_{\ddot{x}_1} + X_{\ddot{\theta}_1} + m_2\ell_1\cos\theta_{10} & I_1 + P_{\ddot{\theta}_1} + m_2\ell_1^2 & -m_2\ell_1\ell_2\cos\theta_{10} \\ -m_2\ell_2 & -m_2\ell_1\ell_2\cos\theta_{10} & I_2 + m_2\ell_2^2 \end{bmatrix},$$

$$\Gamma = \begin{bmatrix} 0 & 0 & 0 \\ 0 & -m_2 g\ell_1\cos\theta_{10} & 0 \\ 0 & 0 & m_2 g\ell_2 \end{bmatrix}.$$

It is noteworthy that the quadratic terms are ignored and the trigonometric functions $\cos\theta_i$ and $\sin\theta_i$ ($i = f,\ 2$) are approximated as $\cos\theta_i \approx 1$ and $\sin\theta_i \approx \theta_i$, respectively, in (11). By taking into account the potential damping and the mechanical friction at hinge, the motion equation (11) can be written as

$$\Xi\ddot{\boldsymbol{p}} + N\dot{\boldsymbol{p}} + \Gamma\boldsymbol{p} = \boldsymbol{Q}, \tag{12}$$

where N is the damping matrix. The external force $\boldsymbol{Q}$ consists of the mooring force, wave excitation force, hydrostatic force and aerodynamics, and can be expressed as

$$\boldsymbol{Q} = \begin{bmatrix} F_x - k(x_1 + \ell_m\sin\theta_1) \\ M_y - \rho g\nabla\overline{\mathrm{GM}}\sin\theta_1 - k(x_1 + \ell_m\sin\theta_1)\ell_m\cos\theta_1 \\ -T_r\ell_2\cos\theta_2 + M_r + F_e d_2\cos\theta_2 + D_e d_2\sin\theta_2 \end{bmatrix}, \tag{13}$$

where k is the linearized restoring coefficient from mooring system, ℓ_m the distance between O_1 and the slewing bearing, A_w and ∇ the water plane area and displacement of the floater, respectively, $\overline{\mathrm{GM}}$ the meta-centric height, d_1 the distance between the rotor plane and O_2, d_2 the distance between the elevator and O_2, F_x and M_y the wave excitation loads on the floater in surge and pitch, respectively, T_r and M_r the thrust and moment on rotor plane, and F_e and D_e the lift and drag force of the elevator. Ignoring the wind speed perturbation, the aero loads are expressed as

$$T_r = \frac{1}{2}\rho_a C_t(\lambda,\beta)AU_\infty^2, \tag{14}$$

$$M_r = \frac{1}{2}\rho_a C_m(\theta_2)ARU_\infty^2 + \frac{1}{2}\rho_a C_c(\lambda,\beta,\gamma)ARU_\infty^2 \tag{15}$$

$$F_e = \frac{1}{2}\rho_a C_l(\alpha,\theta_2)A_e U_\infty^2, \tag{16}$$

$$D_e = \frac{1}{2}\rho_a C_d(\alpha,\theta_2)A_e U_\infty^2, \tag{17}$$

where α is the elevator angle (with respect to the nacelle), γ the cyclic pitch angle, A_e the elevator area, C_l and C_d the lift and drag coefficients of the elevator, respectively. The term M_r consists of the moment generated by the wind-shroud misalignment and the moment generated by the rotor cyclic pitch angle.

Suppose that the rotor rotational speed and the collective pitch β are reserved for wind turbine power regulation and not applied for attitude control, the coefficients C_l, C_d, C_m and C_c can be approximated as

$$C_l(\alpha, \theta_2) \approx a_0 \cdot (\alpha + \theta_2), \tag{18}$$

$$C_d(\alpha, \theta_2) \approx b_0, \tag{19}$$

$$C_m(\theta_2) \approx \left.\frac{dC_m}{d\theta_2}\right|_{\theta_2=0} \theta_2, \tag{20}$$

$$C_c(\lambda, \beta, \gamma) \approx \left.\frac{\partial C_c}{\partial \gamma}\right|_{(\lambda,\beta,0)} \gamma. \tag{21}$$

where a_0 and b_0 are constant and assigned by $a_0 = 5.73$ and $b_0 = 0.01$ since the cross-section of the elevator is thin and symmetric [24]. The combination $(\lambda,\ \beta)$ is the operational point of the wind turbine under the wind speed U_∞.

From (15) and (20), it is noteworthy that the restoring coefficient of the nacelle pitch motion is dependent on the aero loads on the shroud, and varies quadratically with wind speed. The natural frequency of the nacelle motion in pitch DOF, therefore, would increase and approach wave-frequency zone. This feature should be taken into consideration during the design procedure to avoid first-order wave excitation.

Based on the equations (12)$\sim$(19), the supporter-lever system can be expressed by the following state-space model:

$$\dot{\boldsymbol{x}} = \mathcal{A}\boldsymbol{x} + \mathcal{B}_1\alpha + \mathcal{B}_2\gamma + \boldsymbol{d}, \tag{22}$$

where $\boldsymbol{x} = [\boldsymbol{p}^T,\ \dot{\boldsymbol{p}}^T]^T$ is the state vector, $\boldsymbol{d}$ is the disturbance including the wave excitation loads. The system matrix $\mathcal{A}$ and output matrices $[\mathcal{B}_1,\ \mathcal{B}_2,\ \mathcal{B}_3]$ can be obtained from Ξ, N, Γ and Q. As the angle and pitching rate can be measured by inertial measurement units, the output can be expressed as

$$\boldsymbol{y} = \mathcal{C}\boldsymbol{x} + \boldsymbol{w}, \tag{23}$$

where $\boldsymbol{y}$ is expressed as $\boldsymbol{y} = [\theta_f,\ \dot{\theta}_f,\ \theta_2,\ \dot{\theta}_2]^T$, $\boldsymbol{w}$ is the noise vector, and $\mathcal{C}$ is the output matrix.

5.2. Damping Coefficients and Model Verification

The parameters used for the numerical model (12) are calculated from the experimental model and the results are listed in Table 4. The damping matrix $\boldsymbol{N}$ is then identified by using the free-decay experimental results via least-square approach [25], and the result is expressed as

$$\boldsymbol{N} = \begin{bmatrix} 1.16 & -0.0782 & 0 \\ -0.0782 & 0.0481 & -0.00219 \\ 0 & -0.00219 & 0.00219 \end{bmatrix}. \tag{24}$$

The comparison between the simulation and experimental results is shown in Fig. 6. It is found that the free decay response can almost be authentically reproduced by the numerical model. Therefore, the parameters set for the model would be proper in this study.

Table 4: Properties of Experimental Model.

Property	Value
Supporter mass m_1 (kg)	1.55
Lever mass m_2 (kg)	0.35
Moment of inertia of supporter in pitch I_1 (kg·m^2)	4.60×10^{-2}
Moment of inertia of lever in pitch I_2 (kg·m^2)	2.75×10^{-3}
Distance between O_1 and hinge ℓ_1 (cm)	53.0
Distance between O_2 and hinge ℓ_2 (cm)	0.75
Distance between O_2 and rotor plane d_1 (cm)	4.0
Distance between O_2 and elevator d_2 (cm)	26.0
Distance between O_1 and slewing bearing d_0 (cm)	17.0
Linearized restoring coefficient in surge k (N/m)	1.02
Floater added mass in surge $X_{\ddot{x}_1}$ (kg)	2.21
Floater added mass in heave $Z_{\ddot{z}_1}$ (kg)	1.88
Floater added moment of inertia in pitch $P_{\ddot{\theta}_1}$ (kg)	0.055
Floater added mass in surge $X_{\ddot{x}_1}$ (kg·m^2)	2.21
Coupled added mass between surge and pitch $X_{\ddot{\theta}_1}$ (kg·m)	-0.24

5.3. Controller Design

In order not to affect the wind energy conversion of the wind turbine, the collective pitch β and the rotor rotational speed is not applied for floater motion control in this study. Moreover, as the elevator is placed on the upwind side of the wind turbine and the operation of the elevator can disturb the fluid flow, the elevator α is not controlled during the operational mode.

The characteristics of the system expressed by (22) and (23) at different wind speeds are shown in Fig. 9. It can be observed that the dc-gains and, to a lesser extent, the poles of the system depend on the wind speeds. In addition, from the frequency response of θ_f shown in Fig. 9(a,c), it can be found that the controllability of θ_f by both γ and α are weak since the dc-gains are very small. Therefore, floater pitch control is not taken into account in this study.

The block diagram of the nacelle pitch control is shown in Fig. 10. The term θ_2^* is the reference of θ_2 and set as $\theta_2^* = 0$. A conditional switch, which is activated based on the wind turbine modes (switches to cyclic pitch in operational mode and to elevator control in parked mode), is applied. In order to isolate the wave-induced motion into the feedback loops, a notch filter expressed by

$$F_n(s) = \frac{s^2 + 2\zeta_n\omega_n s + \omega_n^2}{s^2 + 2\omega_n s + \omega_n^2}, \tag{25}$$

is performed to remove the wave-frequency components in θ_2. The terms ω_n and ζ_n are the parameters to be designed. Usually, ω_n is set close to the wave frequency and ζ_n is a parameter used to control the magnitude of the notch.

PD (Proportional-Derivative) controllers:

$$C_p(s) = K_p + K_d s, \tag{26}$$

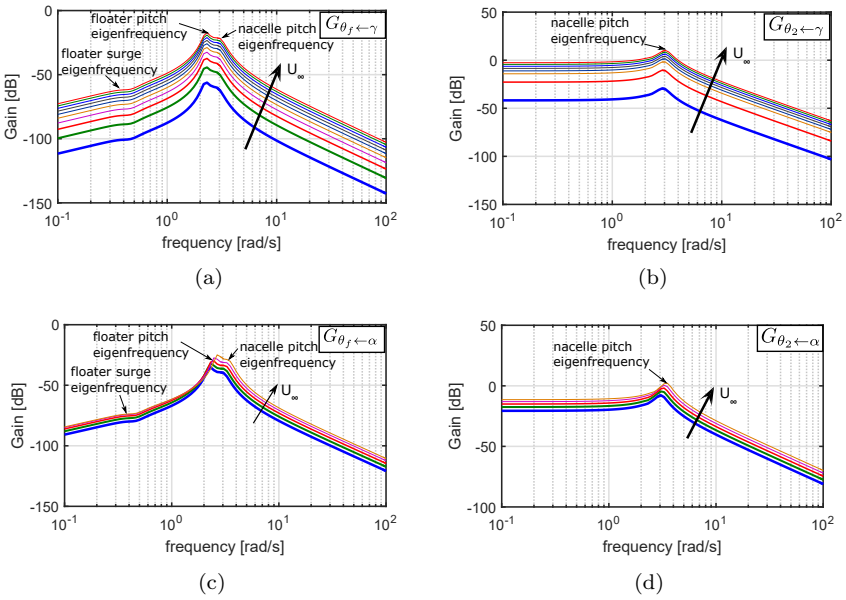

Figure 9: Amplitude diagram of the frequency response with respect to γ and α under turbine's operational mode.

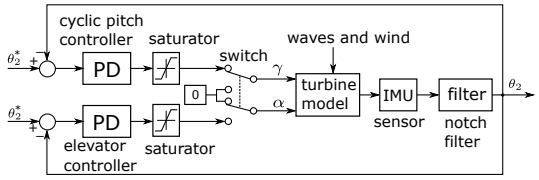

Figure 10: Block diagram of control system.

where K_p and K_d are the tuning parameters, are designed to regulate the damping ratio and natural angular frequency of the closed-loop systems. As the characteristics of θ_2 are dependent on wind speeds, gain-scheduling approach which designing controllers at several different conditions and tuning the PD parameters in accordance to wind speed would be proper for the control. In the following, nacelle pitch control under operational and parked modes are discussed.

5.4. Nacelle Attitude Control Results

The operational mode with wind speed of 1.6 m/s and the parked mode with wind speed of 4.0 m/s are studied. The terms ζ_n and ω_n are set as $\zeta_n = 0.2$ and $\omega_n = 7.0$ rad/s for the notch filter (25). The parameters of PD controller are tuned to let the damping ratio and natural frequency of the nacelle be 0.2 and 4.0 rad/s, respectively. The cyclic pitch and the elevator angle are set to

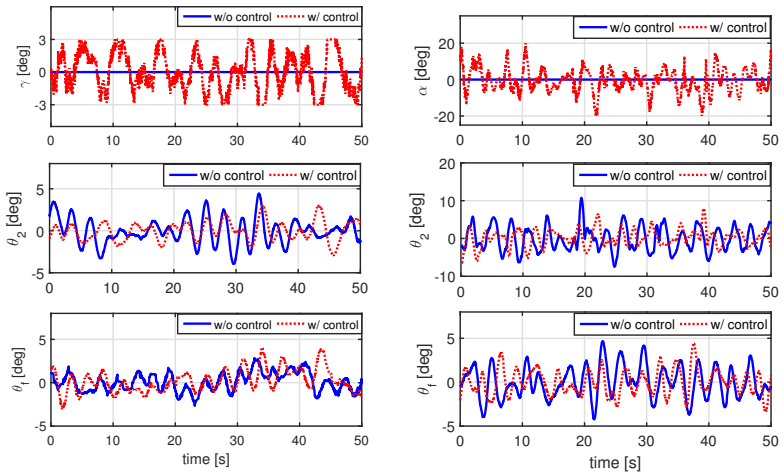

(a) Operational mode (wind speed 1.6 m/s). (b) Parked mode (wind speed 4.0 m/s).

Figure 11: Experimental results with and without control. The upper graphs show the control input, middle graphs show the nacelle pitch, and lower graphs show the floater pitch. The solid lines are the results without control and the dotted lines are the results with control.

Table 5: Standard deviation of attitude motion.

	operational mode		parked mode	
	w/o control	w/ control	w/o control	w/ control
θ_2 [deg]	1.51	1.47	3.28	2.35
θ_f [deg]	1.20	1.52	1.80	1.68

vary in $[-3,\ 3]$ deg and $[-20,\ 20]$, respectively. The experimental results with and without control are plotted in Fig. 11. As floater pitch motion exerts large influence on nacelle motion, the floater pitch is also plotted in the figure for a better comparison. The statistical analysis of the results are compared in Fig. 12 and Table 5. In both turbine modes, the nacelle pitch motion can be reduced slightly according to the statistical results. It is noteworthy that the actuators are saturated in large nacelle motion and limit the control performance. Therefore, a study on exploring the trade-off between the nacelle stabilization (rotor cyclic pitch control) and wind power conversion (rotor collective pitch control) would be necessary.

In the experiments, especially under large wind speeds, collision between the shroud and the tower occurred occasionally. For instance, the sharp changes of θ_2 near 20 s and 40 s in Fig. 11(b) are caused by the collision. Therefore, additional mechanism would be necessary to damper/limit the hinge so as to protect the system from mechanical damage.

It is also noteworthy that in order to satisfy the scaling rule of the model, lightweight digital servos, which are low resolution and low bandwidth, are

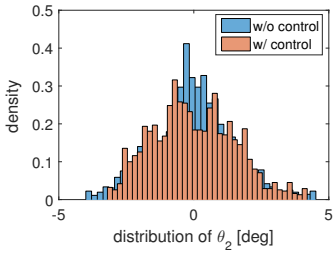

(a) Histogram plot of θ_2 under operational mode.

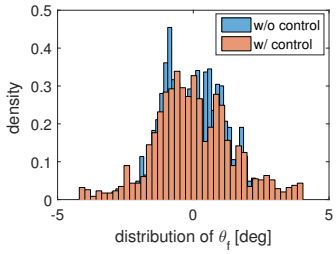

(b) Histogram plot of θ_f under operational mode.

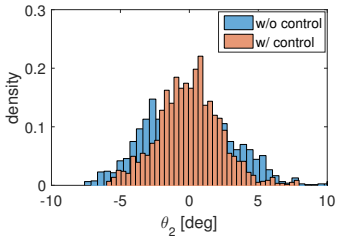

(c) Histogram plot of θ_2 under parked mode.

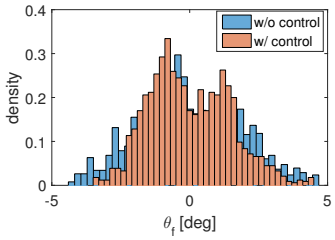

(d) Histogram plot of θ_f under parked mode.

Figure 12: Histogram plot of the model's attitude motion.

applied to regulate the cyclic pitch and elevator. Therefore, the control performance would be expected to be improved when high-performance actuators are applied. Moreover, it can be obtained from the equation (18) that θ_2 causes a positive feedback in attitude control (which can weaken the control performance of elevator). The elevator is required to move with a large swing range during the control, which not only reduce the control performance but also the life-span of the actuator. Therefore, a new design to place the elevator at the downwind side of the nacelle would be a better consideration.

6. Conclusion

This paper provided a fundamental study on a novel floating type shrouded wind turbine via model tests. The quasi-steady performance and the aero-hydro dynamics of the wind turbine were explored by wind-tunnel experiments and wave basin experiments, respectively. In addition, a linear numerical model was derived for the nacelle attitude controller design. From the study, it can be obtained:

- The self-aligning performance for tracking wind direction can be obtained under a wind-wind turbine misalignment of 150^o even without rudder control.

- In low and moderate wind speeds, waves would be the leading cause of the turbine motion. Therefore, floating foundation with cylindrical components, not the square shaped pontoons applied in this study, would be a better solution.

- Active control can help on reducing the nacelle motion in both operational and parked modes. However, in order not to disturb the wind power conversion, the range of cyclic pitch is limited. This can also limit the capacity of the controller on nacelle attitude regulation.

In addition, from the experiments, several attention should be paid for the next phase of study:

- The rudder and elevator would be preferred to be placed at the downwind side of the nacelle since it can improve the stability performance of the nacelle and reduce the operational range of the actuators.

- The natural frequency of the nacelle motion is largely dependent on wind speeds owing to the restoring moment on the shroud. Systematic design of the wind turbine considering the environmental conditions of the installation field is necessary to avoid first-order wave excitation.

According to the study, remediation efforts on the design are necessary for improving the aero-hydro-servo performance. Future work for the floating shrouded wind turbine will also span over the applications for remote areas and offshore fishery industries with no utility grid. Independent power source by integrating the turbine with batteries could potentially be beneficial for the small wind turbine market.

Acknowledgment

This research was partially supported by JSPS KAKENHI Grant No. 26420826.

[1] IEA., Average annual growth rates of world renewables supply, 1990-2018, http://www.iea.org, [accessed on 24/Jun./2021] (2020).

[2] IRENA., Global energy transformation: A roadmap to 2050 (2019 edition) (2019).

[3] IEA., Technology roadmap: Wind energy 2013 edition, http://www.iea.org, [accessed on 26/April/2021] (2013).

[4] IRENA., Future of wind: Deployment, investment, technology, grid integration and socio-economic aspects (a global energy transformation paper) (2019).

[5] D. G. Phillips, An investigation on diffuser augmented wind turbine design, Ph.D. thesis, Doctoral dissertation, ResearchSpace@Auckland (2003).

[6] A. Agha, H. N. Chaudhry, F. Wang, Determining the augmentation ratio and response behaviour of a diffuser augmented wind turbine (dawt), Sustainable Energy Technologies and Assessments 37 (2020) 100610.

[7] R. Bontempo, R. Carandente, M. Manna, A design of experiment approach as applied to the analysis of diffuser-augmented wind turbines, Energy Conversion and Management 235 (2021) 113924.

[8] K. Watanabe, Y. Ohya, A simple theory and performance prediction for a shrouded wind turbine with a brimmed diffuser, Energies 14 (12) (2021) 3661.

[9] F. Bet, H. Grassmann, Upgrading conventional wind turbines, Renewable Energy 28 (1) (2003) 71–78.

[10] Y. Ohya, T. Karasudani, A shrouded wind turbine generating high output power with wind-lens technology, Energies 3 (4) (2010) 634–649.

[11] A. Agha, H. N. Chaudhry, F. Wang, Diffuser augmented wind turbine (DAWT) technologies: a review, International Journal of Renewable Energy Research (IJRER) 8 (3) (2018) 1369–1385.

[12] J. R. Vaz, D. H. Wood, Aerodynamic optimization of the blades of diffuser-augmented wind turbines, Energy Conversion and Management 123 (2016) 35–45.

[13] N. K. Siavash, G. Najafi, T. T. Hashjin, B. Ghobadian, E. Mahmoodi, An innovative variable shroud for micro wind turbines, Renewable Energy 145 (2020) 1061–1072.

[14] J. Bukala, K. Damaziak, H. R. Karimi, K. Kroszczynski, M. Krzeszowiec, J. Malachowski, Modern small wind turbine design solutions comparison in terms of estimated cost to energy output ratio, Renewable Energy 83 (2015) 1166–1173.

[15] K. Watanabe, Y. Ohya, T. Uchida, T. Nagai, Numerical prediction and field verification test of wind-power generation potential in nearshore area using a moored floating platform, Journal of Flow Control, Measurement & Visualization 5 (2) (2017) 21–35.

[16] C. Hu, M. Sueyoshi, C. Liu, Y. Liu, et al., Hydrodynamic analysis of a semi-submersible type floating wind turbine, in: The Eleventh ISOPE Pacific/Asia Offshore Mechanics Symposium, International Society of Offshore and Polar Engineers, 2014.

[17] N. K. Siavash, B. Ghobadian, G. Najafi, A. Rohani, T. Tavakoli, E. Mahmoodi, R. Mamat, et al., Prediction of power generation and rotor angular speed of a small wind turbine equipped to a controllable duct using artificial neural network and multiple linear regression, Environmental research 196 (2021) 110434.

[18] J.-F. Hu, W.-X. Wang, Upgrading a shrouded wind turbine with a self-adaptive flanged diffuser, Energies 8 (6) (2015) 5319–5337.

[19] S. N. Leloudas, G. N. Lygidakis, A. I. Eskantar, I. K. Nikolos, A robust methodology for the design optimization of diffuser augmented wind turbine shrouds, Renewable Energy 150 (2020) 722–742.

[20] H. Zhu, M. Sueyoshi, C. Hu, S. Yoshida, A study on a floating type shrouded wind turbine: Design, modeling and analysis, Renewable Energy 134 (2019) 1099–1113.

[21] H. Zhu, M. Sueyoshi, C. Hu, S. Yoshida, Modelling and attitude control of a shrouded floating offshore wind turbine with hinged structure in extreme conditions, in: Proceedings of the IEEE 6th International Conference on Renewable Energy Research and Applications (ICRERA), San Diego, 2017.

[22] Fukushima Offshore Wind Consortium, Joint probobility distribution of wave height and wave period, http://www.fukushima-forward.jp/english/deta/index.html, [accessed on 11/May/2021] (2021).

[23] T. I. Fossen, Handbook of marine craft hydrodynamics and motion control, John Wiley & Sons, Ltd, UK, 2011.

[24] T. Burton, N. Jenkins, D. Sharpe, E. Bossanyi, Wind energy handbook, John Wiley & Sons, 2011.

[25] J. Dalzell, A note on the form of ship roll damping., Tech. rep., STEVENS INST OF TECH HOBOKEN NJ DAVIDSON LAB (1976).